Impacts of aerosol-photolysis interaction and aerosol-radiation feedback on surface-layer ozone in North China during a multi-pollutant air pollution episode

Hao Yang[1], Lei Chen[1], Hong Liao[1], Jia Zhu[1], Wenjie Wang[2], Xin Li[2]

[1]Jiangsu Key Laboratory of Atmospheric Environment Monitoring and Pollution Control, Jiangsu Collaborative Innovation Center of Atmospheric Environment and Equipment Technology, School of Environmental Science and Engineering, Nanjing University of Information Science & Technology, Nanjing 210044, China

[2]State Joint Key Laboratory of Environmental Simulation and Pollution Control, College of Environmental Sciences and Engineering, Peking University, Beijing 100871, China

Correspondence: Lei Chen (chenlei@nuist.edu.cn) and Hong Liao (hongliao@nuist.edu.cn)

Abstract

We examined the impacts of aerosol-radiation interactions, including the effects of aerosol-photolysis interaction (API) and aerosol-radiation feedback (ARF), on surface-layer ozone (O_3) concentrations during one multi-pollutant air pollution episode characterized by high O_3 and $PM_{2.5}$ levels from 28 July to 3 August 2014 in North China, by using the Weather Research and Forecasting with Chemistry (WRF-Chem) model embedded with an integrated process analysis scheme. Our results show that aerosol-radiation interactions decreased the daytime shortwave radiation at surface by 93.2 W m^{-2} averaged over the complex air pollution areas. The dimming effect reduced the 2 m temperature and near-surface photolysis rates of $J[NO_2]$ and $J[O^1D]$ by 0.56 °C, 1.8×10^{-3} s^{-1} and 6.1×10^{-6} s^{-1}, respectively. However, the daytime shortwave radiation in the atmosphere was increased by 72.8 W m^{-2}, which made the atmosphere more stable. The stabilized atmosphere decreased the planetary boundary layer height and 10 m wind speed by 129.0 m and 0.12 m s^{-1}, respectively, and increased the relative humidity at 2 m by 2.4%. The weakened photolysis rates and changed meteorological conditions reduced daytime surface-layer O_3 concentrations by up to 11.4 ppb (13.5%), with API and ARF contributing 74.6% and 25.4% of the O_3 decrease, respectively. Process analysis indicated that the weakened O_3 chemical production made the greatest contribution to API effect while the reduced vertical mixing was the key process for ARF effect. This study implies that future $PM_{2.5}$ reductions will lead to O_3 increases due to weakened aerosol-radiation interactions. Therefore, tighter controls of O_3 precursors are needed to offset O_3 increases caused by weakened aerosol-radiation interactions in the future.

1 Introduction

China has been experiencing severe air pollution in recent years, characterized by high loads of $PM_{2.5}$ (particulate matter with an aerodynamic equivalent diameter of 2.5 micrometers or less) and high levels of ozone (O_3). Observational studies exhibited positive correlations and synchronous occurrence of $PM_{2.5}$ and O_3 pollution in North China during summer (Zhao et al., 2018; Zhu et al., 2019), indicating that complex air pollution is becoming a major challenge for North China.

Aerosols can absorb and scatter solar radiation to affect Earth's energy balance. They can also act as cloud condensation nuclei and ice nuclei, and further modify the microphysical characteristics of clouds (Albrecht et al., 1989; Haywood et al., 2000; Lohmann et al., 2005). Both ways perturb meteorological variables, e.g., temperature, planetary boundary layer height (PBLH), and precipitation, and eventually influence air pollutants (Petäjä et al., 2016; Miao et al., 2018; Zhang et al., 2018). Many studies are focused on the feedback between aerosol and meteorology (Gao et al., 2015; Gao et al., 2016a; Qiu et al., 2017; Chen et al., 2019; Zhu et al., 2021). Gao et al. (2015) used the WRF-Chem model to investigate the feedbacks between aerosols and meteorological variables over the North China Plain in January 2013, and pointed out that aerosols could cause a decrease in surface temperature by 0.8-2.8 °C but an increase of 0.1-0.5 °C around 925 hPa. The more stable atmosphere caused by surface cooling and higher-layer heating led to the decreases of surface wind speed and PBLH by 0.3 m s^{-1} and 40-200 m, respectively, which further resulted in overall $PM_{2.5}$ increases by 10-50 μg m^{-3} (2-30%). By using the same WRF-Chem model, Qiu et al. (2017) reported that the surface downward shortwave radiation and PBLH were reduced by 54.6 W m^{-2} and 111.4 m due to aerosol radiative forcing during 21 and 27 February 2014 in the North China Plain. As a result, the surface $PM_{2.5}$ concentration averaged over the North China Plain was increased by 34.9 μg m^{-3} (20.4%).

Aerosols can also influence O_3 through aerosol-radiation interactions, including aerosol-photolysis interaction and aerosol-radiation feedback. Aerosols can scatter and absorb UV radiation, and therefore directly affect O_3 photochemistry reactions, which

70   is called aerosol-photolysis interaction (API) (Dickerson et al., 1997; Liao et al., 1999;

71   Li et al., 2011; Lou et al., 2014). The changed meteorological variables due to aerosol

72   radiative forcing can indirectly affect O_3 concentrations, which is called aerosol-

73   radiation feedback (ARF) (Hansen et al., 1997; Gao et al., 2018; Liu et al., 2020).

74   Although the effects of API or ARF on O_3 have been examined by previous studies

75   (Xing et al., 2017; Gao et al., 2018; Gao et al., 2020), the combined effects of API and

76   ARF on O_3, especially under the conditions of synchronous occurrence of high $PM_{2.5}$

77   and O_3 concentrations, remain largely elusive.

78   The present study aims to (1) quantify the respective/combined contributions of

79   API and ARF on surface O_3 concentrations by using the WRF-Chem model; (2) explore

80   the prominent physical and/or chemical processes responsible for API and ARF effects

81   by using an integrated process rate (IPR) analysis embedded in WRF-Chem model. The

82   analysis is conducted during one multi-pollutant air pollution episode characterized by

83   high O_3 and $PM_{2.5}$ levels from 28 July to 3 August 2014 in North China. The model

84   configuration, numerical experiments, observational data, and the integrated process

85   rate analysis are described in section 2. Section 3 shows the model evaluation. The

86   presentation of the model results and the corresponding analyses are exhibited in

87   section 4. The discussion is provided in section 5, and the conclusion and uncertainties

88   of this study are given in section 6.

89   2 Methods

90   2.1 Model configuration

91   The version 3.7.1 of the online-coupled Weather Research and Forecasting with

92   Chemistry (WRF-Chem) model (Grell et al., 2005; Skamarock et al., 2008) is used in

93   this study to explore the impacts of aerosol-radiation interactions on surface-layer O_3

94   in North China. WRF-Chem can simulate gas phase species and aerosols coupled with

95   meteorological fields, and has been widely used to investigate air pollution over North

96   China (Gao et al., 2016a; Gao et al., 2020; Wu et al., 2020). As shown in Fig. 1, we

97   design two nested model domains with the number of grid points of 57 (west–east) ×

98   41 (south–north) and 37 (west–east) × 43 (south–north) at 27 and 9 km horizontal

99 resolutions, respectively. The parent domain centers at 39 °N, 117 °E. The model

100 contains 29 vertical levels from the surface to 50 hPa, with 14 levels below 2 km for

101 the fully description of the vertical structure of planetary boundary layer (PBL).

102 The Carbon Bond Mechanism Z (CBM-Z) is selected as the gas-phase chemical

103 mechanism (Zaveri and Peters, 1999), and the full 8-bin MOSAIC (Model for

104 Simulating Aerosol Interactions and Chemistry) aerosol module with aqueous

105 chemistry is used to simulate aerosol evolution (Zaveri et al., 2008). The photolysis

106 rates are calculated by the Fast-J scheme (Wild et al., 2000). Other major physical

107 parameterizations used in this study are listed in Table 1.

108 The initial and boundary meteorological conditions are provided by the National

109 Centers for Environmental Prediction (NCEP) Final Analysis data with a spatial

110 resolution of $1° \times 1°$. In order to limit the model bias of simulated meteorological fields,

111 the four-dimensional data assimilation (FDDA) is used with a nudging coefficient of

112 3.0×10^{-4} for the wind, temperature and humidity (no analysis nudging is applied for

113 the inner domain) (Lo et al., 2008; Otte, 2008). Chemical initial and boundary

114 conditions are obtained from the Model for Ozone and Related chemical Tracers,

115 version 4 (MOZART-4) forecasts (Emmons et al., 2010).

116 Anthropogenic emissions are taken from the 2010 MIX Asian emission inventory

117 (Li et al., 2017a), which provides emissions of sulfur dioxide (SO_2), nitrogen oxides

118 (NO_x), carbon monoxide (CO), non-methane volatile organic compounds (NMVOCs),

119 carbon dioxide (CO_2), ammonia (NH_3), black carbon (BC), organic carbon (OC), PM_{10}

120 (particulate matter with aerodynamic diameter is 10 µm and less) and $PM_{2.5}$. Emissions

121 are aggregated from four sectors, including power generation, industry, residential, and

122 transportation, with $0.25° \times 0.25°$ spatial resolution. Biogenic emissions are calculated

123 online by the Model of Emissions of Gases and Aerosols from Nature (MEGAN)

124 (Guenther et al., 2006).

125 **2.2 Numerical experiments**

126 To quantify the impacts of API and ARF on O_3, three case simulations have been

127 conducted: (1) BASE – the base simulation coupled with the interactions between

aerosol and radiation, which includes both impacts of API and ARF; (2) NOAPI – the same as the BASE case, but the impact of API is turned off (aerosol optical properties are set to zero in the photolysis module), following Wu et al. (2020); (3) NOALL – both the impacts of API and ARF are turned off (removing the mass of aerosol species when calculating aerosol optical properties in the optical module), following Qiu et al. (2017). The differences between BASE and NOAPI (i.e., BASE minus NOAPI) represent the impacts of API. The contributions from ARF can be obtained by comparing NOAPI and NOALL (i.e., NOAPI minus NOALL). The combined effects of API and ARF on O_3 concentrations can be quantitatively evaluated by the differences between BASE and NOALL (i.e., BASE minus NOALL).

Each simulation is conducted from 26 July to 3 August 2014, with the first 40 hours as the model spin-up. Simulation results from the BASE case during 28 July and 3 August 2014 are used to evaluate the model performance.

2.3 Observational data

Simulation results are compared with meteorological and chemical measurements. The surface-layer meteorological data (2 m temperature (T_2), 2 m relative humidity (RH_2), and 10 m wind speed (WS_{10})), with a temporal resolution of 3 h, at ten stations (Table S1) are obtained from NOAA's National Climatic Data Center (https://gis.ncdc.noaa.gov/maps/ncei/cdo/hourly). The radiosonde data of temperature at 08:00 and 20:00 LST in Beijing (39.93 °N, 116.28 °E) are provided by the University of Wyoming (http://weather.uwyo.edu/). Observed hourly concentrations of $PM_{2.5}$ and O_3 at thirty-two sites (Table S2) in North China are collected from the China National Environmental Monitoring Center (CNEMC). The photolysis rate of nitrogen dioxide (NO_2) ($J[NO_2]$) measured at the Peking University site (39.99 °N, 116.31 °E) is also used to evaluate the model performance. More details about the measurement technique of $J[NO_2]$ can be found in Wang et al. (2019). The satellite-retrieved 550 nm AOD products from the Moderate Resolution Imaging Spectroradiometer (MODIS) are also used to compare with the simulated ones. The model results from 10:00 to 11:00 and 13:00 to 14:00 LT are extracted and averaged, due to instruments on board the Terra

157 and Aqua platforms pass over China at around 10:30 and 13:30 LT, respectively.

2.4 Integrated process rate analysis

159   Integrated process rate (IPR) analysis has been widely used to quantify the

160 contributions of different processes to O_3 variations (Goncalves et al., 2009; Gao et al.,

161 2016b; Tang et al., 2017; Gao et al., 2018). In this study, four physical/chemical

162 processes are considered, including vertical mixing (VMIX), net chemical production

163 (CHEM), horizontal advection (ADVH), and vertical advection (ADVZ). VMIX is

164 initiated by turbulent process and closely related to PBL development, which influences

165 O_3 vertical gradients. CHEM represents the net O_3 chemical production (chemical

166 production minus chemical consumption). ADVH and ADVZ represent transport by

167 winds (Gao et al., 2016b). In this study, we define ADV as the sum of ADVH and ADVZ.

3 Model evaluation

169   Reasonable representation of observed meteorological and chemical variables by

170 the WRF-Chem model can provide foundation for evaluating the impacts of aerosols

171 on surface-layer ozone concentration. The model results presented in this section are

172 taken from the BASE case. The concentrations of air pollutants are averaged over the

173 thirty-two observation sites in Beijing, Tianjin and Baoding. To ensure the data quality,

174 the mean value for each time is calculated only when concentrations are available at

175 more than sixteen sites.

3.1 Chemical simulations

177   Figure 2 shows the spatial-temporal variations of observed and simulated $PM_{2.5}$

178 and O_3 concentrations over North China during 28 July to 3 August 2014. The observed

179 higher concentrations in Beijing and Baoding than those in Tianjin are well reproduced

180 by WRF-Chem. The model can also reasonably capture the temporal variations of

181 observed $PM_{2.5}$ and O_3 with correlation coefficients (R) of 0.66 for $PM_{2.5}$ and 0.86 for

182 O_3, although simulated results underestimate the observed $PM_{2.5}$ by -19.2% and O_3 by

183 -12.0%. The failure to reproduce $PM_{2.5}$ peak values may be attributed to incomplete

184 treatments of chemical reactions in WRF-Chem, e.g., The failure to reproduce $PM_{2.5}$

185 peak values may be attributed to incomplete treatments of chemical reactions in WRF-

186 Chem, e.g., missing the heterogeneous chemistry in the model (Cheng et al., 2016) and

187 the lack of secondary organic aerosols (SOA) formation pathways in the aerosol module

188 (Chen et al., 2019). More statistical parameters between simulations and observations

189 are presented in Table 2.

190 Figure S1 shows the spatial distributions of aerosol optical depth (AOD) at 550

191 nm retrieved from MODIS and simulated by WRF-Chem during 28 July to 3 August

192 2014. In the WRF-Chem model, the AOD at 550 nm are calculated by using the values

193 at 400 and 600 nm according to the Ångstrom exponent. Analyzing Fig. S1, the model

194 can well reproduce the spatial distribution of observed AOD but slightly underestimate

195 the value. The spatial correlation coefficient between the simulated and observed AOD

196 is 0.98.

197 **3.2 Meteorological simulations**

198 Figure 3 shows the time series of observed and simulated T_2, RH_2, and WS_{10}

199 averaged over ten meteorological observation stations, and $J[NO_2]$ at Peking University

200 during 28 July to 3 August 2014. The statistical metrics for T_2, RH_2, WS_{10}, and $J[NO_2]$

201 are also presented in Table 2. Generally, the model can depict the temporal variations

202 of T_2 fairly well with R of 0.98 and the mean bias (MB) of -1.5 °C. For RH_2, the R and

203 MB are 0.91 and 0.5%, respectively. Although WRF-Chem model overestimates WS_{10}

204 with the MB of 0.7 m s^{-1}, the R for WS_{10} is 0.89 and the root-mean-square error (RMSE)

205 is 0.9 m s^{-1}, which is smaller than the threshold of model performance criteria (2 m s^{-1})

206 proposed by Emery et al. (2001). The large positive bias in wind speed was also

207 reported in other studies (Zhang et al., 2010; Gao et al., 2015; Liao et al., 2015; Qiu et

208 al., 2017). The predicted $J[NO_2]$ agrees well with the observations with R of 0.97 and

209 NMB of 6.8%. We also conduct comparison between observed and simulated

210 temperature profiles at 08:00 and 20:00 LST in Beijing during 29 July to 1 August 2014

211 in Figure S2. The vertical profile of observed temperature, especially the thermal

212 inversion layer occurred on 31 July around 1600 m, is well captured by the model.

213 Generally, the WRF-Chem model reasonably reproduces the temporal variations of

214   observed meteorological parameters.

4 Results

216   It is known that co-occurrence of $PM_{2.5}$ and O_3 pollution is frequently observed
217   nowadays over China (Dai et al., 2021). The complex air pollution characterized by
218   high $PM_{2.5}$ and O_3 levels has already received widespread attention from both scientists
219   and policy-makers. Therefore, we examine the impacts of aerosol-radiation interactions
220   on O_3 concentrations with a special focus on the complex air pollution areas (CAPAs,
221   Fig. S3), where the mean simulated daily $PM_{2.5}$ and MDA8 (maximum daily 8-h
222   average) O_3 concentrations are larger than 75 µg m^{-3} and 80 ppb, respectively, based
223   on the National Ambient Air Quality Standards (http://www.mee.gov.cn).

4.1 Impacts of aerosol-radiation interactions on meteorology

225   Figure 4 shows the impacts of aerosol-radiation interactions on shortwave
226   radiation at the surface (BOT_SW), shortwave radiation in the atmosphere (ATM_SW),
227   PBLH, T_2, RH_2, and WS_{10} during the daytime (08:00-17:00 LST) from 28 July to 3
228   August 2014. As a result of the interactions between aerosol and radiation (the
229   combined impacts of API and ARF), BOT_SW is decreased over the entire simulated
230   domain. Over CAPAs, the BOT_SW is decreased by 93.2 W m^{-2} (20.5%). Contrary to
231   the changes in BOT_SW, ATM_SW is increased significantly with an increase of 72.8
232   W m^{-2} (25.3%) over CAPAs. The decreased BOT_SW perturbs the near-surface energy
233   flux, which weakens convection and suppresses the development of PBL (Li et al.,
234   2017b). The PBLH averaged over CAPAs is calculated to decrease by 129.0 m (13.0%).
235   The reduced surface radiation budget can directly lead to changes in near-surface
236   temperature. Therefore, the changes in T_2 have the similar spatial patterns with
237   BOT_SW; the surface temperature is decreased by 0.56 °C averaged over CAPAs. RH_2
238   is increased over most of the domain with an average rise of 2.4%, which is beneficial
239   for the hygroscopic growth of aerosols. WS_{10} exhibits overall reductions over CAPAs
240   and is calculated to decrease by 0.12 m s^{-1} on average. We also examine the changed
241   meteorological variables caused by API and ARF respectively. As shown in Fig. S4,
242   API has little impact on meteorological variables; the above changes are mainly caused

243 by ARF.

4.2 Impacts of aerosol-radiation interactions on photolysis

245 Figure 5 shows the spatial distribution of mean daytime surface-layer $PM_{2.5}$

246 concentrations simulated by BASE case and the changes in $J[NO_2]$ and $J[O^1D]$ due to

247 aerosol-radiation interactions from 28 July to 3 August 2014. When the combined

248 impacts (API and ARF) are considered, $J[NO_2]$ and $J[O^1D]$ are decreased over the entire

249 domain; the spatial patterns of changed $J[NO_2]$ and $J[O^1D]$ are similar to that of

250 simulated $PM_{2.5}$. The surface $J[NO_2]$ and $J[O^1D]$ are decreased by 1.8×10^{-3} s^{-1} (40.5%)

251 and 6.1×10^{-6} s^{-1} (48.8%) averaged over CAPAs. Figure S5 exhibits the percentage

252 changes in surface $J[NO_2]$ and $J[O^1D]$ caused by API and ARF respectively. It is found

253 that $J[NO_2]$ and $J[O^1D]$ are significantly modified by API and little affected by ARF.

4.3 Impacts of aerosol-radiation interactions on O_3

255 Figure 6 shows the changes in surface-layer O_3 due to API, ARF, and the combined

256 effects (denoted as ALL). As shown in Fig. 6a, API alone leads to overall surface O_3

257 decreases over the entire domain with an average reduction of 8.5 ppb (10.1%) over

258 CAPAs. The change can be explained by the substantially diminished UV radiation due

259 to aerosol loading, which significantly weakens the efficiency of photochemical

260 reactions and restrains O_3 formation. The decreased surface O_3 concentration due to

261 ARF, however, is only 2.9 ppb (3.1%, Fig. 6b), which indicates that API is the dominant

262 way for O_3 reduction related to aerosol-radiation interactions. The combined effects of

263 API and ARF are shown in Fig. 6c. Generally, aerosol-radiation interactions decrease

264 the surface O_3 concentration by 11.4 ppb (13.5%) averaged over CAPAs.

4.4 Influencing mechanism of aerosol-radiation interactions on O_3

266 Figure 7a shows diurnal variations of simulated surface (first layer) daytime O_3

267 concentrations over CAPAs in three cases (BASE, NOAPI, and NOALL). All cases

268 present O_3 increases from 08:00 LST. It is shown that the simulated O_3 concentrations

269 in BASE case increase more slowly than that in NOAPI and NOALL cases. To explain

270 the underlying mechanisms of API and ARF impacts on O_3, we quantify the variations

271 in contributions of different processes (ADV, CHEM, and VMIX) to O_3 by using the

272   IPR analysis.

273   Figure 7b shows hourly surface O_3 changes induced by each physical/chemical

274   process (i.e., ADV, CHEM, and VMIX) in BASE case. The significant positive

275   contribution to the hourly variation in O_3 is contributed by VMIX, and the contribution

276   reaches the maximum at about 10:00 LST. After 14:00 LST, the contribution from

277   VMIX remains constant (nearly +2 ppb h^{-1}), which is probably attributed to the stable

278   boundary layer development (Tang et al., 2016). The CHEM process makes negative

279   contributions at around 09:00 and 16:00 LST, which means that the chemical

280   consumption of O_3 is stronger than the chemical production. At noon, the net chemical

281   contribution turns to be positive due to stronger solar UV radiation. The contribution

282   from all the processes (NET, the sum of VMIX, CHEM, and ADV) to O_3 is peaked at

283   the noon and then becomes weakened. After sunset (17:00 LST), the NET contribution

284   turns to be negative over CAPAs, leading to O_3 decrease.

285   Figure 7c shows the changes in hourly process contributions caused by API. The

286   chemical production of O_3 is suppressed significantly due to aerosol impacts on

287   photolysis rates. The weakened O_3 chemical production decreases the contribution from

288   CHEM, and results in a negative value of CHEM_DIF (-3.5 ppb h^{-1}). In contrast to

289   CHEM_DIF, the contribution from changed VMIX (VMIX_DIF) to O_3 concentration

290   due to API is always positive, and the mean value is +3.1 ppb h^{-1}. The impact of API

291   on ADV process is relatively small (-0.36 ppb h^{-1}). NET_DIF, namely the sum of

292   VMIX_DIF, CHEM_DIF and ADV_DIF, indicates the differences in hourly O_3 changes

293   caused by API. As shown in Fig. 7c, NET_DIF is almost negative during the daytime

294   over CAPAs with the mean value of -0.76 ppb h^{-1}. This is because the decreases in

295   CHEM and ADV are larger than the increases in VMIX caused by API; the O_3 decrease

296   is mainly attributed to the significantly decreased contribution from CHEM. The

297   maximum difference in O_3 between BASE and NOAPI appears at 17:00 LST with a

298   value of -10.1 ppb (Fig. 7a).

299   Figure 7d shows the impacts of ARF on each physical/chemical process

300   contribution to the hourly O_3 variation. At 08:00 LST, the change in VMIX due to ARF

301   is large with a value of -4.6 ppb h^{-1}, resulting in a net negative variation with all

302 processes considered. The decrease in O_3 reaches the maximum with the value of 6.1

303 ppb at around 09:00 LST over CAPAs (Fig. 7a). During 10:00 to 16:00 LST, the positive

304 VMIX_DIF (mean value of +0.59 ppb h^{-1}) or the positive CHEM_DIF (mean value of

305 +0.16 ppb h^{-1}) is the major process to positive NET_DIF.

306 When both impacts of API and ARF are considered, the variation pattern of the

307 difference in hourly process contribution shown in Fig. 7e is similar to that in Fig. 7c,

308 which indicates that API is the dominant factor to surface-layer O_3 reduction.

309 Figure 8 presents the vertical profiles of simulated daytime O_3 concentrations in

310 three cases (BASE, NOAPI, and NOALL), and the differences in contributions from

311 each physical/chemical process to hourly O_3 variations caused by API, ARF and the

312 combined effects during 28 July to 3 August 2014 over CAPAs. As shown in Fig. 8a,

313 the O_3 concentration is lower in BASE than that in other two scenarios (NOAPI and

314 NOALL), especially at the lower 12 levels (below 731.9 m), owing to the impacts of

315 aerosols (API and/or ARF).

316 The changes in each process contribution caused by API are presented in Fig. 8b.

317 The contribution from CHEM_DIF is -2.14 ppb h^{-1} for first seven layers (from 23.4 to

318 290.7 m). Conversely, the contribution from VMIX_DIF shows a positive value under

319 the 290.7 m (between first layer to seventh layer) with the mean value of +1.7 ppb h^{-1}.

320 The positive variation in VMIX due to API may be associated with the different vertical

321 gradient of O_3 between BASE and NOAPI cases. The contributions of changed

322 advections (ADVH_DIF and ADVZ_DIF) are relatively small, with mean values of

323 +0.25 and -0.47 ppb h^{-1} respectively below the first seven layers, which may result from

324 small impact of API on wind filed (Fig. S4a). The net difference is a negative value (-

325 0.66 ppb h^{-1}); API leads to O_3 reduction not only nearly surface but also aloft.

326 Figure 8c shows the differences in O_3 budget due to ARF. When the ARF is

327 considered, the vertical turbulence is weakened and the development of PBL is

328 inhibited, which makes VMIX_DIF negative at the lower 7 layers (below the 290.7 m)

329 with a mean value of -0.55 ppb h^{-1}, but the variation in CHEM caused by ARF is

330 positive with a mean value of +0.6 ppb h^{-1}. The enhanced O_3 precursors due to ARF

331 can promote the chemical production of O_3 (Tie et al., 2009). The changes of ADVZ

332 and ADVH (ADVZ_DIF and ADVH_DIF) caused by ARF are associated with the

333 variations in wind filed. When ARF is considered, the horizontal wind speed is

334 decreased (Fig. S6a), which makes ADVH_DIF positive at the lower twelve layers with

335 a mean value of $+0.5$ ppb h^{-1}. However, ADVZ_DIF is negative at these layers with a

336 mean value of -0.48 ppb h^{-1} because aerosol radiative effects decrease the transport of

337 O_3 from the upper to lower layers (Fig. S6b).

338   In Fig. 8d, the pattern and magnitude of the differences in process contributions

339 between BASE and NOALL are similar to those caused by API, indicating again the

340 dominate role of API on O_3 changes. The impacts of API on O_3 both near the surface

341 and aloft are greater than those of ARF.

5 Discussions

343   In order to make the analysis and conclusions more robust, another two complex

344 air pollution episodes (8-13 July 2015 and 5-11 June 2016) in this region are also

345 selected to conduct simulations for generating general conclusions. Simulated air

346 pollutants (PM$_{2.5}$ and O_3) and meteorological variables (T$_2$, RH$_2$, and WS$_{10}$) during 8-

347 13 July 2015 (Episode 2) and 5-11 June 2016 (Episode 3) are compared with

348 observations (Fig. S7-Fig. S8). In general, both the observed meteorological parameters

349 and pollutant concentrations can be reasonably reproduced by the model, with

350 correlation coefficients (R) of 0.56~0.98 and normalized mean bias (NMB) of –

351 7.1%~+33.4%. More details about the model evaluation are listed in the supporting

352 information (Text S1).

353   As shown in Fig. S9(a1-a2), API alone leads to the decrease in surface O_3 over the

354 entire domain with an average reduction of 9.0 ppb (10.6%) and 8.3 ppb (10.4%) over

355 CAPAs in Episode 2 and Episode 3, respectively. The decreased surface O_3

356 concentrations over CAPAs due to ARF are only 1.0 ppb (1.2%, Fig. 9(b1)) and 1.0 ppb

357 (1.1%, Fig. 9(b2)) during Episode 2 and Episode 3, respectively. All the results indicate

358 that API is the dominant factor for O_3 reduction related to aerosol-radiation interactions,

359 the same as the conclusion analyzed from the case during 28 July to 3 August 2014.

360 The combined effects of API and ARF decrease surface O_3 by 10.0 ppb (11.9%) and

9.3 ppb (11.6%) over CAPAs in Episode 2 and Episode 3, respectively. Analyzing Fig. S10 and Fig. S11, similar variation characteristics are shown in Episode 2 and Episode 3 as that during 28 July to 3 August 2014, with the larger impacts of API on O_3 both near the surface and aloft than those of ARF, indicating the dominant role of API on O_3 reduction related with aerosol-radiation interactions.

6 Conclusions

In this study, the fully coupled regional chemistry transport model WRF-Chem is applied to investigate the impacts of aerosol-radiation interactions, including the impact of aerosol-photolysis interaction (API) and the impact of aerosol-radiation feedback (ARF), on O_3 during a summertime complex air pollution episode from 28 July to 3 August 2014. Three sensitivity experiments are designed to quantify the respective and combined impacts from API and ARF. Generally, the spatiotemporal distributions of observed pollutant concentrations and meteorological parameters are captured fairly well by the model with high correlation coefficients of 0.66–0.86 for pollutant concentrations and 0.70–0.98 for meteorological parameters.

Sensitivity experiments show that aerosol-radiation interactions decrease BOT_SW, T_2, WS_{10}, PBLH, $J[NO_2]$, and $J[O^1D]$ by 93.2 W m^{-2}, 0.56 °C, 0.12 m s^{-1}, 129 m, 1.8×10^{-3} s^{-1}, and 6.1×10^{-6} s^{-1} over CAPAs, and increase ATM_SW and RH_2 by 72.8 W m^{-2} and 2.4%. The changed meteorological variables and weakened photochemistry reaction further reduce surface-layer O_3 concentration by up to 11.4 ppb (13.5%), with API and ARF contributing 74.6% and 25.4%, respectively.

We further examine the influencing mechanism of aerosol-radiation interactions on O_3 by using integrated process rate analysis. API can directly affect O_3 by reducing the photochemistry reactions within the lower several hundred meters and therefore amplify the O_3 vertical gradient, which promotes the vertical mixing of O_3. The reduced photochemistry reactions of O_3 weaken the chemical contribution and reduce surface O_3 concentrations, even though the enhanced vertical mixing can partly counteract the reduction. ARF affects O_3 concentrations indirectly through the changed meteorological variables, e.g., the decreased PBLH. The suppressed PBL can weaken

390   the vertical mixing of O_3 by turbulence. Generally, the impacts of API on O_3 both near

391   the surface and aloft are greater than those of ARF, indicating the dominant role of API

392   on O_3 reduction related with aerosol-radiation interactions.

393   This study provides a detailed understanding of aerosol impacts on O_3 through

394   aerosol-radiation interactions (including both API and ARF). The results imply that

395   future $PM_{2.5}$ reductions will lead to O_3 increases due to weakened aerosol-radiation

396   interactions. A recent study emphasized the need for controlling VOCs emissions to

397   mitigate O_3 pollution (Li et al., 2019). Therefore, tighter controls of O_3 precursors

398   (especially VOCs emissions) are needed to counteract future O_3 increases caused by

399   weakened aerosol-radiation interactions, and the contributions of different mitigation

400   strategies with the impacts of aerosol-radiation interactions to O_3 air quality will be

401   discussed detailedly in our future work.

402   There are some limitations to this work. The uncertainty of the lack of secondary

403   organic aerosols (SOA), and the missing mechanisms of some heterogeneous reactions

404   may result in large uncertainties in the final simulation results. Gao et al. (2017) added

405   some SOA formation mechanisms into the MOSAIC module by using the volatility

406   basis set (VBS) in WRF-Chem and found that the surface $PM_{2.5}$ concentrations in urban

407   Beijing were reduced by 1.9 μg m^{-3} due to the weakened ARF effect during Asia-Pacific

408   Economic Cooperation (APEC). Similar magnitude can also be found in Zhou et al.

409   (2019) (-1.8 μg m^{-3}) who did not consider the impacts of SOA in WRF-Chem when

410   analyzing the impacts of weakened ARF on $PM_{2.5}$ during APEC. Therefore, more work

411   should be conducted to explore the impacts of ARF on $PM_{2.5}$ and O_3 concentrations

412   under consideration of SOA in future.

413

Data availability

The observed hourly surface concentrations of air pollutants are derived from the China National Environmental Monitoring Center (http://www.cnemc.cn). The observed surface meteorological data are obtained from NOAA's National Climatic Data Center (https://gis.ncdc.noaa.gov/maps/ncei/cdo/hourly). The radiosonde data are provided by the University of Wyoming (http://weather.uwyo.edu/). The photolysis rates of nitrogen dioxide in Beijing are provided by Xin Li (li_xin@pku.edu.cn). The MODIS data are obtained from the NASA Level 1 and Atmosphere Archive and Distribution System (https://ladsweb.modaps.eosdis.nasa.gov). The simulation results can be accessed by contacting Lei Chen (chenlei@nuist.edu.cn) and Hong Liao (hongliao@nuist.edu.cn).

Author contributions

HY, LC, and HL conceived the study and designed the experiments. HY and LC performed the simulations and carried out the data analysis. JZ, WW, and XL provided useful comments on the paper. HY prepared the paper with contributions from all co-authors.

Competing interests

The authors declare that they have no competing interests.

Acknowledgements

This work is supported by the National Key R&D Program of China (2019YFA0606804), the National Natural Science Foundation of China (42007195), and the Meteorological Soft Science Program of China Meteorological Administration (2021ZZXM46). We acknowledge the High Performance Computing Center of Nanjing University of Information Science & Technology for their support of this work.

Reference

Albrecht, B. A.: Aerosols, cloud microphysics, and fractional cloudiness, Science, 245, 1227–1230, 1989.

Chen, F. and Dudhia, J.: Coupling an Advanced Land Surface – Hydrology Model with the Penn State – NCAR MM5 Modeling System. Part I: Model Implementation and Sensitivity, Mon. Weather Rev., 129(4), 569–585, 2001.

Chen, L., Zhu, J., Liao, H., Gao, Y., Qiu, Y., Zhang, M., Liu, Z., Li, N., and Wang, Y.: Assessing the formation and evolution mechanisms of severe haze pollution in the Beijing–Tianjin–Hebei region using process analysis, Atmos. Chem. Phys., 19, 10845–10864, https://doi.org/10.5194/acp-19-10845-2019, 2019.

Cheng, Y., Zheng, G., Chao, W., Mu, Q., Bo, Z., Wang, Z., Meng, G., Qiang, Z., He, K., and Carmichael, G.: Reactive nitrogen chemistry in aerosol water as a source of sulfate during haze events in China, Science Advances, 2, https://doi.org/10.1126/sciadv.1601530, 2016.

Dai, H., Zhu, J., Liao, H., Li, J., Liang, M., Yang, Y., and Yue, X.: Co-occurrence of ozone and $PM_{2.5}$ pollution in the Yangtze River Delta over 2013–2019: Spatiotemporal distribution and meteorological conditions, Atmos. Res., 249, 105363, 2021.

Dickerson, R. R., Kondragunta, S., Stenchikov, G., Civerolo, K. L., Doddridge, B. G., and Holben, B. N.: The impact of aerosols on solar ultraviolet radiation and photochemical smog, Science, 278, 827-830, 10.1126/science.278.5339.827, 1997.

Emery, C., Tai, E., and Yarwood, G.: Enhanced meteorological modeling and performance evaluation for two Texas ozone episodes, in: Prepared for the Texas Natural Resource Conservation Commission, ENVIRON International Corporation, Novato, CA, USA, 2001.

Emmons, L. K., Walters, S., Hess, P. G., Lamarque, J.-F., Pfister, G. G., Fillmore, D., Granier, C., Guenther, A., Kinnison, D., Laepple, T., Orlando, J., Tie, X., Tyndall, G., Wiedinmyer, C., Baughcum, S. L., and Kloster, S.: Description and evaluation of the Model for Ozone and Related chemical Tracers, version 4 (MOZART-4), Geosci.

Model Dev., 3, 43–67, doi:10.5194/gmd- 3-43-2010, 2010.

Foken, T.: 50 years of the Monin-Obukhov similarity theory, Bound.-Layer Meteor., 119, 431–437, 2006.

Gao, J., Li, Y., Zhu, B., Hu, B., Wang, L., and Bao, F.: What have we missed when studying the impact of aerosols on surface ozone via changing photolysis rates?, Atmos. Chem. Phys., 20, 10831–10844, https://doi.org/10.5194/acp-20-10831-2020, 2020.

Gao, J. H., Zhu, B., Xiao, H., Kang, H. Q., Pan, C., Wang, D. D., and Wang, H. L.: Effects of black carbon and boundary layer interaction on surface ozone in Nanjing, China, Atmos. Chem. Phys., 18, 7081–7094, https://doi.org/10.5194/acp-18-7081-2018, 2018.

Gao, M., Carmichael, G. R., Wang, Y., Saide, P. E., Yu, M., Xin, J., Liu, Z., and Wang, Z.: Modeling study of the 2010 regional haze event in the North China Plain, Atmos. Chem. Phys., 16, 1673–1691, doi:10.5194/acp-16-1673-2016, 2016a.

Gao, J., Zhu, B., Xiao, H., Kang, H., Hou, X., and Shao, P.: A case study of surface ozone source apportionment during a high concentration episode, under frequent shifting wind conditions over the Yangtze River Delta, China, Sci. Total Environ., 544, 853, https://doi.org/10.1016/j.scitotenv.2015.12.039, 2016b.

Gao, M., Liu, Z., Wang, Y., Lu, X., Ji, D. and Wang, L.: Distinguishing the roles of meteorology, emission control measures, regional transport, and co-benefits of reduced aerosol feedbacks in "APEC" Blue, Atmos. Environ., 167, 476–486, 420 doi:10.1016/j.atmosenv.2017.08.054, 2017.

Gao, Y., Zhang, M., Liu, Z., Wang, L., Wang, P., Xia, X., Tao, M., and Zhu, L.: Modeling the feedback between aerosol and meteorological variables in the atmospheric boundary layer during a severe fog–haze event over the North China Plain, Atmos. Chem. Phys., 15, 4279–4295, doi:10.5194/acp-15-4279-2015, 2015.

Goncalves, M., Jimenez-Guerrero, P., Baldasano, J.M.: Contribution of atmospheric processes affecting the dynamics of air pollution in South-Western Europe during a typical summertime photochemical episode, Atmos. Chem. Phys., 9, 849 – 864, doi:10.5194/acp-9-849-2009, 2009.

Grell, G. A., Peckham, S. E., Schmitz, R., Mckeen, S. A., Frost, G., Skamarock, K., and Eder, B.: Fully coupled "online" chemistry within the WRF model, Atmos. Environ., 39, 6957–6975, 2005.

Guenther, A., Karl, T., Harley, P., Wiedinmyer, C., Palmer, P. I., and Geron, C.: Estimates of global terrestrial isoprene emissions using MEGAN (Model of Emissions of Gases and Aerosols from Nature), Atmos. Chem. Phys., 6, 3181–3210, doi:10.5194/acp-6-3181-2006, 2006.

Hansen, J., Sato, M., and Ruedy, R.: Radiative forcing and climate response, J. Geophys. Res., 102, 6831–6864, 1997.

Haywood, J. and Boucher, O.: Estimates of the direct and indirect radiative forcing due to tropospheric aerosols: A review, Rev. Geophys., 38, 513–543, 2000.

Hong, S.-Y., Noh, Y., and Dudhia, J.: A New Vertical Diffusion Package with an Explicit Treatment of Entrainment Processes, Mon. Weather Rev., 134, 2318–2341, 2006.

Iacono, M. J., Delamere, J. S., Mlawer, E. J., Shephard, M. W., Clough, S. A., and Collins, W. D.: Radiative forcing by long-lived greenhouse gases: Calculations with the AER radiative transfer models, J. Geophys. Res., 113, D13103, doi:10.1029/2008JD009944, 2008.

Li, G., Bei, N., Tie, X., and Molina, L. T.: Aerosol effects on the photochemistry in Mexico City during MCMA-2006/MILAGRO campaign, Atmos Chem Phys, 11, 5169-5182, 10.5194/acp-11-5169-2011, 2011.

Li, K., Jacob, D. J., Liao, H., Zhu, J., Shah, V., Shen, L., Bates, K. H., Zhang, Q., and Zhai, S.: A two-pollutant strategy for improving ozone and particulate air quality in China, Nat. Geosci., 12, 906–910, https://doi.org/10.1038/s41561-019-0464-x, 2019.

Li, M., Zhang, Q., Kurokawa, J.-I., Woo, J.-H., He, K., Lu, Z., Ohara, T., Song, Y., Streets, D. G., Carmichael, G. R., Cheng, Y., Hong, C., Huo, H., Jiang, X., Kang, S., Liu, F., Su, H., and Zheng, B.: MIX: a mosaic Asian anthropogenic emission inventory under the international collaboration framework of the MICS-Asia and HTAP, Atmos. Chem. Phys., 17, 935–963, https://doi.org/10.5194/acp-17-935-2017, 2017a.

Li, Z., Guo, J., Ding, A., Liao, H., Liu, J., Sun, Y., Wang, T., Xue, H., Zhang, H., and Zhu, B.: Aerosol and boundary-layer interactions and impact on air quality, Nat. Sci. Rev., 4, 810–833, https://doi.org/10.1093/nsr/nwx117, 2017b.

Liao, H., Yung, Y. L., and Seinfeld, J. H.: Effects of aerosols on tropospheric photolysis rates in clear and cloudy atmospheres, J. Geophys. Res., 104, 23697–23707, 1999.

Liao, L., Lou, S. J., Fu, Y., Chang, W. Y., and Liao, H.: Radiative forcing of aerosols and its impact on surface air temperature on the synoptic scale in eastern China [in Chinese], Chin. J. Atmos. Sci., 39, 68–82, doi: 10.3878/j.issn.1006-9895.1402.13302, 2015.

Lin, Y.-L., Farley, R. D., and Orville, H. D.: Bulk parameterization of the snow field in a cloud model, J. Clim. Appl. Meteorol., 22, 1065–1092, 1983.

Liu, Y. and Wang, T.: Worsening urban ozone pollution in China from 2013 to 2017 – Part 1: The complex and varying roles of meteorology, Atmos. Chem. Phys., 20, 6305–6321, https://doi.org/10.5194/acp-20-6305-2020, 2020.

Lo, J. C.-F., Yang, Z. L., and Pielke Sr, R. A.: Assessment of three dynamical climate downscaling methods using the Weather Research and Forecasting (WRF) model, J. Geophys. Res., 113, D09112, doi:10.1029/2007jd009216, 2008.

Lohmann, U., and Feichter, J.: Global indirect aerosol effects: A review. Atmospheric Chemistry and Physics, 5, 715–737, https://doi.org/10.5194/acp-5-715-2005, 2005.

Lou, S., Liao, H., and Zhu, B.: Impacts of aerosols on surface-layer ozone concentrations in China through heterogeneous reactions and changes in photolysis rates, Atmos. Environ., 85, 123–138, 2014.

Miao, Y., Liu, S., Guo, J., Huang, S., Yan, Y., and Lou, M.: Unraveling the relationships between boundary layer height and $PM_{2.5}$ pollution in China based on four-year radiosonde measurements, *Environmental Pollution*, https://doi.org/10.1016/j.envpol.2018.09.070, 2018.

Otte, T. L.: The impact of nudging in the meteorological model for retrospective air quality simulations. Part I: Evaluation against national observation networks. J. Appl. Meteor. Climatol., 47, 1853–1867, 2008.

Petäjä, T., Järvi, L., Kerminen, V. M., Ding, A. J., Sun, J. N., Nie, W., Kujansuu, J.,

560 Virkkula, A., Yang, X., Fu, C. B., Zilitinkevich, S., and Kulmala, M.: Enhanced air

561   pollution via aerosol-boundary layer feedback in China, Sci. Rep., 6, 18998,

562   doi:10.1038/srep18998, 2016.

563 Qiu, Y., Liao, H., Zhang, R., and Hu, J.: Simulated impacts of direct radiative effects

564   of scattering and absorbing aerosols on surface layer aerosol concentrations in China

565   during a heavily polluted event in February 2014, J. Geophys. Res. Atmos., 122,

566   5955–5975, doi:10.1002/2016JD026309, 2017.

567 Skamarock, W., Klemp, J. B., Dudhia, J., Gill, D. O., Barker, D. M., Duda, M., Huang,

568   X. Y., Wang,W., and Powers, J. G.: A description of the advanced research WRF

569   version 3, NCAR technical note NCAR/TN/u2013475, 2008.

570 Tang, G. Q., Zhu, X.W., Xin, J. Y., Hu, B., Song, T., Sun, Y., Zhang, J. Q., Wang, L. L.,

571   Cheng, M. T., Chao, N., Kong, L. B., Li, X., and Wang, Y. S.: Modelling study of

572   boundary-layer ozone over northern China – Part I: Ozone budget in summer, Atmos.

573   Res., 187, 128–137, 2017.

574 Tang, G., Zhang, J., Zhu, X., Song, T., Münkel, C., Hu, B., Schäfer, K., Liu, Z., Zhang,

575   J., Wang, L., Xin, J., Suppan, P., and Wang, Y.: Mixing layer height and its

576   implications for air pollution over Beijing, China, Atmos. Chem. Phys., 16, 2459–

577   2475, doi:10.5194/acp-16-2459-2016, 2016.

578 Tie, X., Geng, F., Li, P., Gao, W., and Zhao, C.: Measurement and modelling of ozone

579   variability in Shanghai, China, Atmos. Environ., 43, 4289–4302, 2009.

580 Wang, W., Li, X., Shao, M., Hu, M., Zeng, L., Wu, Y., and Tan, T.: The impact of

581   aerosols on photolysis frequencies and ozone production in Beijing during the 4-year

582   period 2012–2015, Atmos. Chem. Phys., 19, 9413–9429,

583   https://doi.org/10.5194/acp19-9413-2019, 2019.

584 Wild, O., Zhu, X., and Prather, M. J.: Fast-J: Accurate simulation of in- and below-

585   cloud photolysis in tropospheric chemical models, J. Atmos. Chem., 37, 245–282,

586   doi:10.1023/A:1006415919030, 2000.

587 Wu, J., Bei, N., Hu, B., Liu, S., Wang, Y., Shen, Z., Li, X., Liu, L., Wang, R., Liu, Z.,

588   Cao, J., Tie, X., Molina, L. T., Li, G.: Aerosol-photolysis interaction reduces

589   particulate matter during wintertime haze events, Proc. Natl. Acad. Sci. USA, 117,

590   9755–9761, 2020.

591   Xing, J., Wang, J. D., Mathur, R., Wang, S. X., Sarwar, G., Pleim, J., Hogrefe, C.,

592   Zhang, Y. Q., Jiang, J. K., Wong, D. and Hao, J. M.: Impacts of aerosol direct effects

593   on tropospheric ozone through changes in atmospheric dynamics and photolysis rates,

594   Atmos. Chem. Phys., 17, 9869–9883, https://doi.org/10.5194/acp-17-9869-2017,

595   2017.

596   Zaveri, R. A. and Peters, L. K.: A new lumped structure photochemical mechanism for

597   large-scale   applications,   J.   Geophys.   Res.,   104,   D23,   30387–30415,

598   https://doi.org/10.1029/1999JD900876, 1999.

599   Zaveri, R. A., Easter, R. C., Fast, J. D., and Peters, L. K.: Model for simulating aerosol

600   interactions   and   chemistry   (MOSAIC),   J.   Geophys.   Res.,   113,   D13204,

601   https://doi.org/10.1029/2007JD008782, 2008.

602   Zhang, X., Zhang, Q., Hong, C. P., Zheng, Y. X., Geng, G. N., Tong, D., Zhang, Y. X.,

603   and Zhang, X. Y.: Enhancement of $PM_{2.5}$ concentrations by aerosol-meteorology

604   interactions over China. Journal of Geophysical Research: Atmospheres,123, 1179–

605   1194, https://doi.org/10.1002/2017JD027524, 2018.

606   Zhang, Y., Wen, X.-Y., and Jang, C. J.: Simulating chemistry– aerosol–cloud–radiation–

607   climate feedbacks over the continental US using the online-coupled Weather

608   Research Forecasting Model with chemistry (WRF/Chem), Atmos. Environ., 44,

609   3568–3582, doi:10.1016/j.atmosenv.2010.05.056, 2010.

610   Zhao, H.; Zheng, Y., and Li, C. Spatiotemporal distribution of $PM_{2.5}$ and O_3 and their

611   interaction during the summer and winter seasons in Beijing, China. Sustainability,

612   10, 4519, 2018.

613   Zhou, M., Zhang, L., Chen, D., Gu, Y., Fu, T.-M., Gao, M., Zhao, Y., Lu, X. and Zhao,

614   B.: The impact of aerosol-radiation interactions on the effectiveness of emission

615   control   measures,   Environmental   Research   Letters,   14(2),   024002,

616   https://doi.org/10.1088/1748-9326/aaf27d, 2019.

617   Zhu, J., Chen, L., Liao, H., and Dang, R.: Correlations between $PM_{2.5}$ and Ozone over

618   China   and   Associated   Underlying   Reasons,   Atmosphere,   352,   1–15,

619   https://doi.org/10.3390/atmos10070352, 2019.

620   Zhu, J., Chen, L., Liao, H., Yang, H., Yang, Y., and Yue, X.: Enhanced $PM_{2.5}$ Decreases

621   and O_3 Increases in China During COVID-19 Lockdown by Aerosol-Radiation

622   Feedback, Geophys. Res. Lett., 48, https://doi.org/10.1029/2020GL090260, 2021.

623

1   **Table 1.** Physical parameterization options used in the simulation.

Options	Schemes
Microphysics scheme	Lin (Purdue) scheme (Lin et al.,1983)
Cumulus scheme	Grell 3D ensemble scheme
Boundary layer scheme	Yonsei University PBL scheme (Hong et al., 2006)
Surface layer scheme	Monin-Obukhov surface scheme (Foken, 2006)
Land-surface scheme	Unified Noah land-surface model (Chen and Dudhia, 2001)
Longwave radiation scheme	RRTMG (Iacono et al., 2008)
Shortwave radiation scheme	RRTMG (Iacono et al., 2008)

1 **Table 2.** Statistical parameters between simulated and observed $PM_{2.5}$ ($\mu g\ m^{-3}$), O_3
2 (ppb), 2 m temperature (T_2, °C), 2 m relative humidity (RH_2, %), 10 m wind speed
3 (WS_{10}, m s^{-1}), and photolysis rate of NO_2 ($J[NO_2]$, s^{-1}) during 28 July to 3 August 2014.

Variables	O[a]	M[a]	R[b]	MB[c]	ME[d]	NMB[e](%)	NME[f](%)	RMSE[g]
$PM_{2.5}$	113.3	90.7	0.66	-21.8	25.2	-19.2	22.2	30.1
O_3	47.7	44.1	0.86	-5.7	15.5	-12.0	32.4	18.2
T_2	28.4	28.0	0.98	-1.5	1.6	-5.7	5.8	1.8
RH_2	70.9	65.7	0.91	0.5	5.3	0.7	7.9	7.0
WS_{10}	2.4	3.0	0.89	0.7	0.8	28.5	32.1	0.9
$J[NO_2]$	1.6×10^{-3}	1.8×10^{-3}	0.97	1.1×10^{-4}	3×10^{-4}	6.8	18.5	5.3×10^{-4}

4 [a]***O*** and ***M*** are the averages for observed and simulated results, respectively. O =

5 $\frac{1}{n}\times\sum_{i=1}^{n}O_i$, $M = \frac{1}{n}\times\sum_{i=1}^{n}M_i$.

6 [b]***R*** is the correlation coefficient between observations and model results. R=

7 $\frac{\sum_{i=1}^{n}|(O_i\text{-}O)\times(M_i\text{-}M)|}{\sqrt{\sum_{i=1}^{n}(O_i\text{-}O)^2\times\sum_{i=1}^{n}(M_i\text{-}M)^2}}$.

8 [c]***MB*** is the mean bias between observations and model results. MB = $\frac{1}{n}\times\sum_{i=1}^{n}(M_i\text{-}$

9 $O_i)$.

10 [d]***ME*** is the mean error between observations and model results. ME = $\frac{1}{n}\times\sum_{i=1}^{n}|M_i\text{-}O_i|$.

11 [e]***NMB*** is the normalized mean bias between observations and model results. NMB =

12 $\frac{1}{n}\times\sum_{i=1}^{n}\frac{M_i\text{-}O_i}{O_i}\times100\%$.

13 [f]***NME*** is normal mean error between observations and model results. NME=

14 $\frac{1}{n}\times\sum_{i=1}^{n}\frac{|M_i\text{-}O_i|}{O_i}\times100\%$.

15 [g]***RMSE*** is the root-mean-square error of observations and model results. RMSE=

16 $\sqrt{\frac{1}{n}\times\sum_{i=1}^{n}(M_i\text{-}O_i)^2}$.

17 In the above O_i and M_i are the hourly observed and simulated data, respectively, and n
18 is the total number of hours.
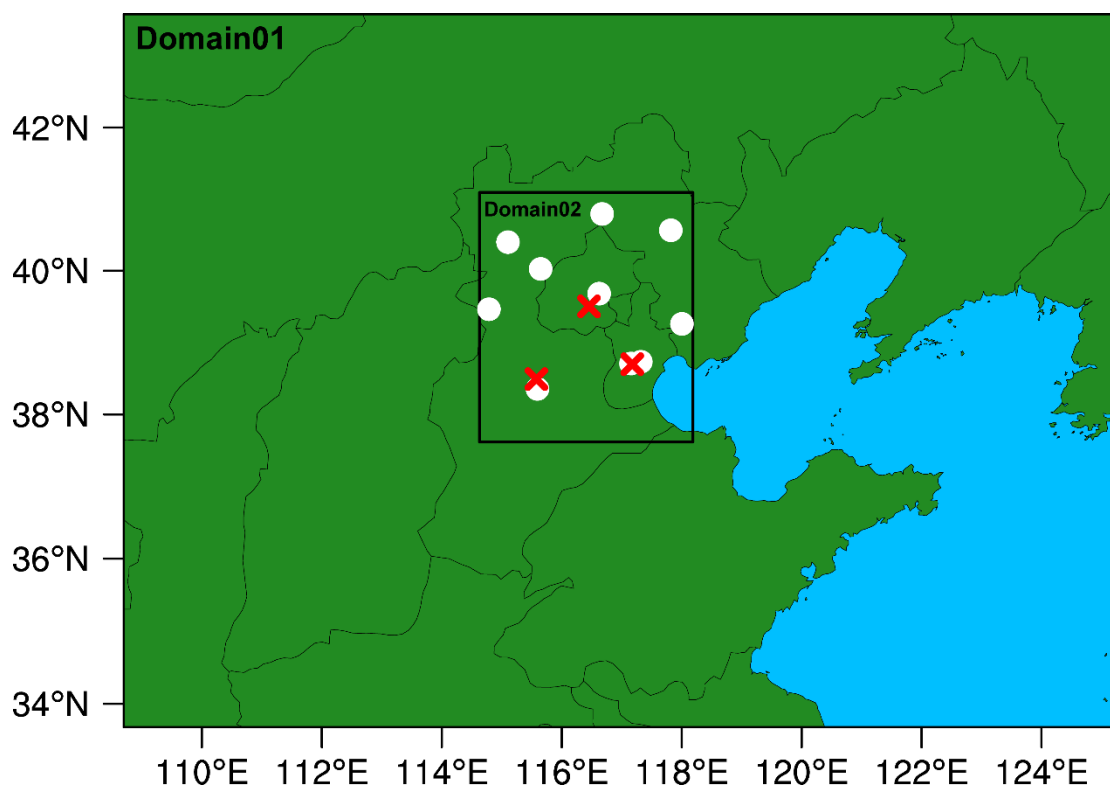
2 **Figure 1.** Map of the two WRF-Chem modeling domains with the locations of
3 meteorological (white dots) and environmental (red crosses) observation sites used for
4 model evaluation.
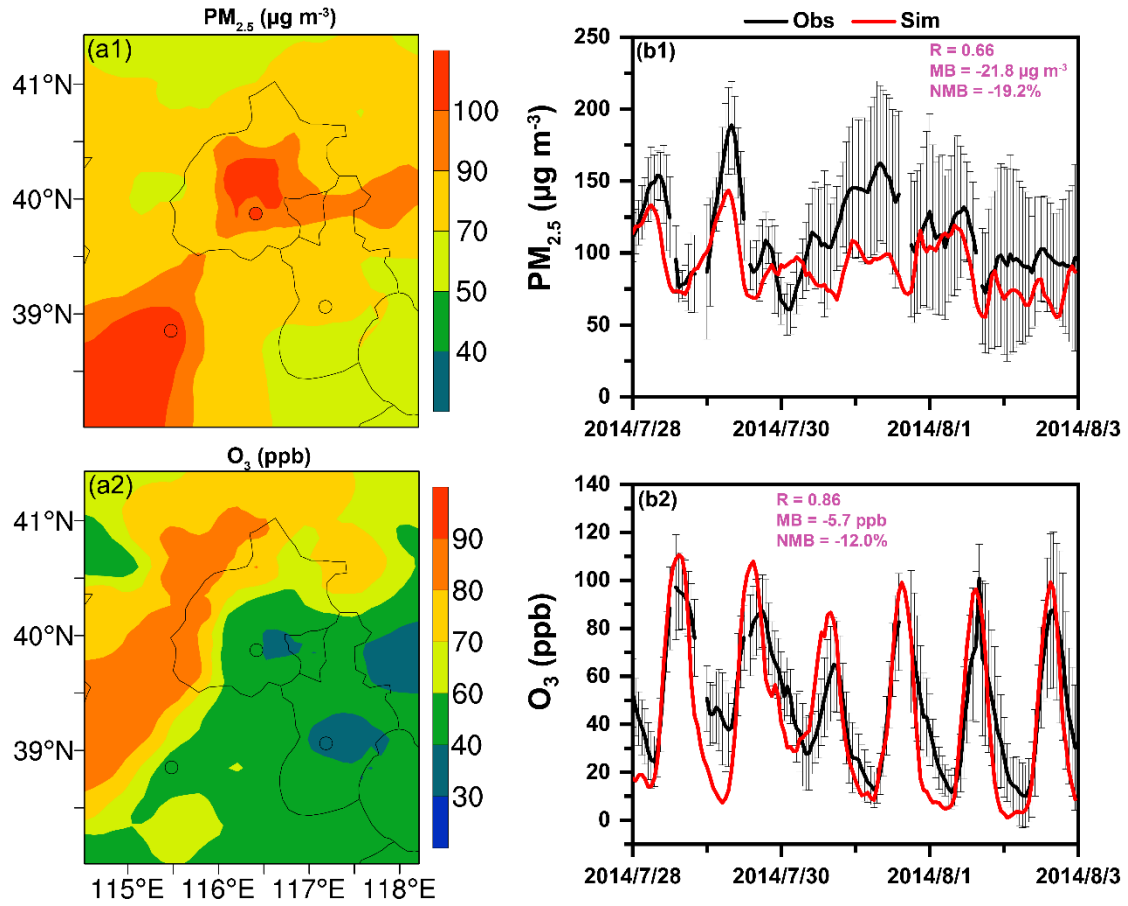
Figure 2. (a1-a2) Spatial distributions of simulated (color counters) and observed (colored circles) surface PM$_{2.5}$ and O$_3$ concentrations averaged during 28 July to 3 August 2014. (b1-b2) Time series of observed (black) and simulated (red) hourly surface PM$_{2.5}$ and O$_3$ concentrations averaged over the thirty-two observation sites in Beijing, Tianjin, and Baoding. The error bars in (b1) and (b2) are standard deviation on those average. The calculated correlation coefficient (R), mean bias (MB), and normalized mean bias (NMB) are also shown.
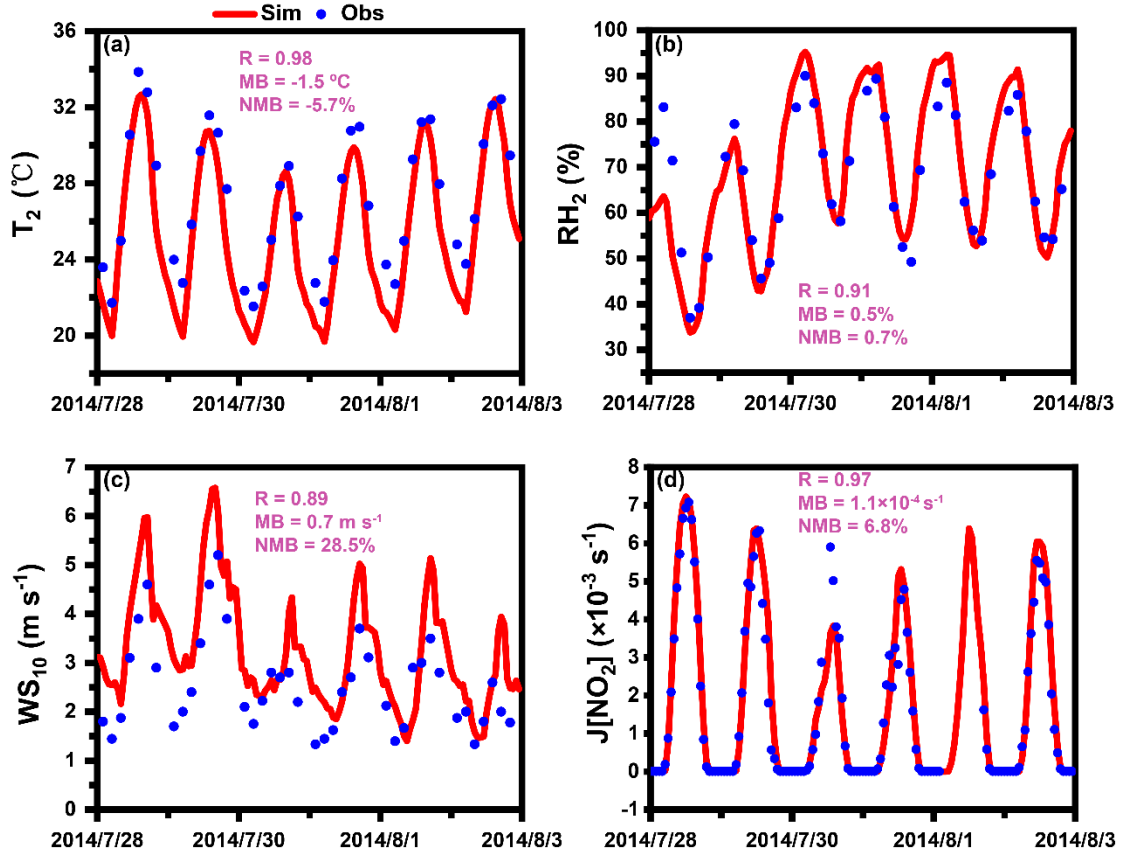
Figure 3. Time series of 3-hourly observed (blue dots) and hourly simulated (red lines)
(a) 2-m temperature (T_2), (b) 2-m relative humidity (RH_2), (c) wind speed at 10 m (WS_{10})
averaged over ten meteorological observation stations, and (d) surface photolysis rate
of NO_2 ($J[NO_2]$) during 28 July to 3 August 2014. The calculated correlation coefficient
(R), mean bias (MB), and normalized mean bias (NMB) are also shown.
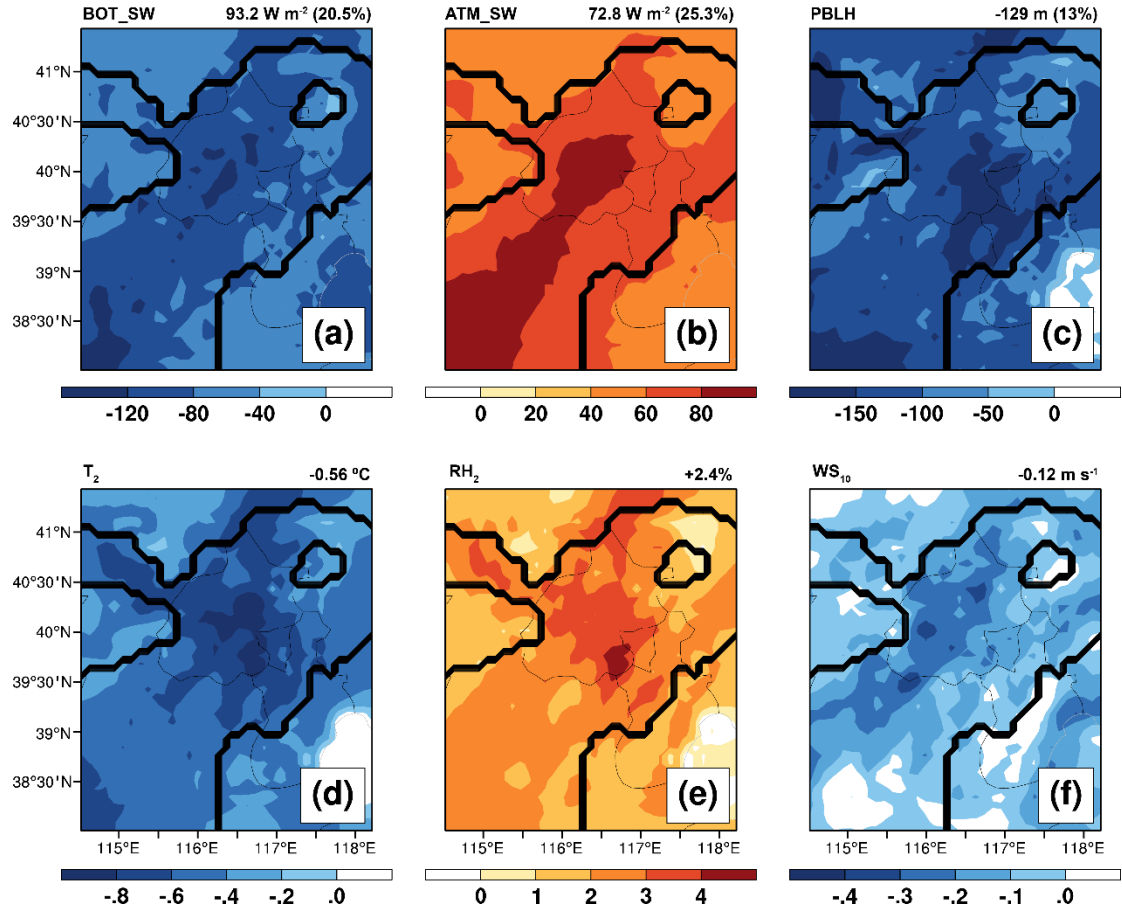
Figure 4. The impacts of aerosol-radiation interactions on (a) shortwave radiation at the surface (BOT_SW), (b) shortwave radiation in the atmosphere (ATM_SW), (c) PBL height (PBLH), (d) 2-m temperature (T_2), (e) 2-m relative humidity (RH_2), and (f) 10-m wind speed (WS_{10}) during the daytime (08:00-17:00 LST) from 28 July to 3 August 2014. The region sandwiched between two black lines is defined as the complex air pollution areas (CAPAs) where the mean daily $PM_{2.5}$ and MDA8 O_3 concentrations in BASE case are larger than 75 µg m^{-3} and 80 ppb. The calculated changes averaged over CAPAs are also shown at the top of each panel.
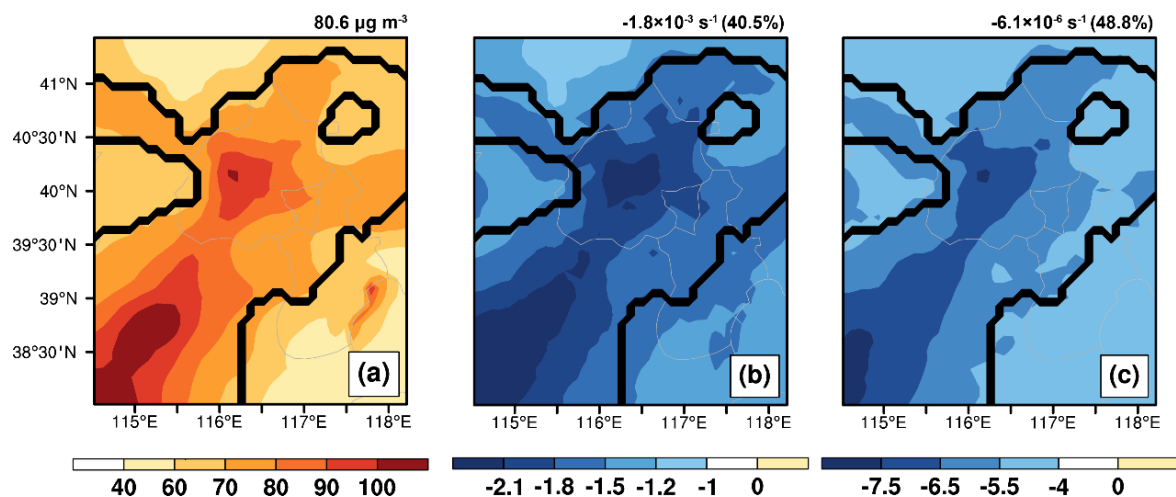
Figure 5. Spatial distributions of (a) simulated surface-layer PM$_{2.5}$ concentrations in BASE case, and changes in surface (b) J[NO$_2$] and (c) J[O^{1}D] due to aerosol-radiation interactions during the daytime (08:00-17:00 LST) from 28 July to 3 August 2014. The calculated values (percentage changes) avaraged over CAPAs are also shown at the top of each panel.
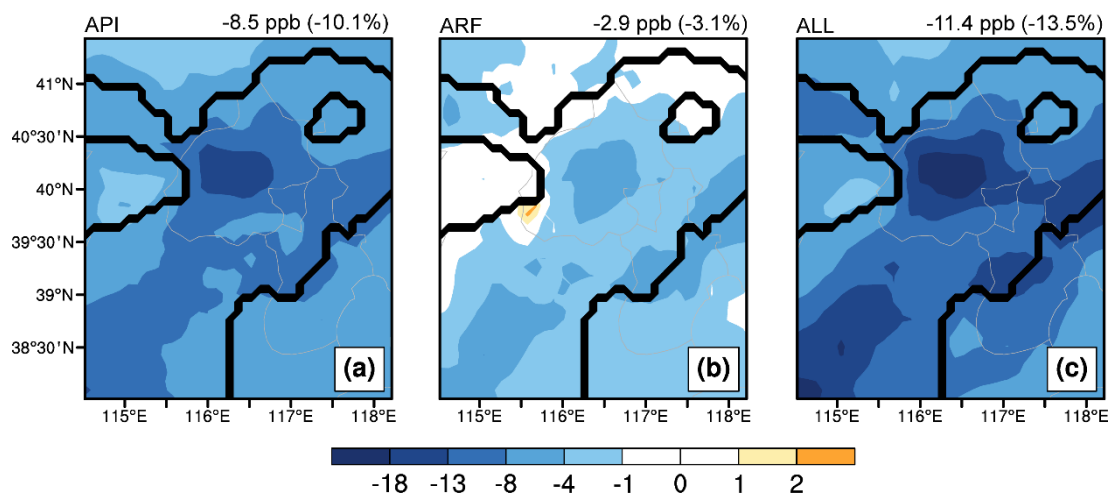
Figure 6. The changes in surface-layer ozone due to (a) aerosol-photolysis interaction (API), (b) aerosol-radiation feedback (ARF), and (c) the combined effects (ALL, defined as API+ARF) during the daytime (08:00-17:00 LST) from 28 July to 3 August 2014. The calculated mean changes avaraged over CAPAs are also shown at the top of each panel.

Figure 7. (a) Diurnal variations of simulated surface O_3 concentrations in BASE (black), NOAPI (blue), and NOALL (red) cases over CAPAs. (b) The hourly surface O_3 changes induced by each physical/chemical process using the IPR analysis method in BASE case. (c-e) Changes in hourly surface O_3 process contributions caused by API (BASE minus NOAPI), ARF (NOAPI minus NOALL), and ALL (BASE minus NOALL) over CAPAs during the daytime (08:00-17:00 LST) from 28 July to 3 August 2014. The black lines with squares denote the net contribution of all processes (NET, defined as VMIX+CHEM+ADV). Differences of each process contribution are denoted as VMIX_DIF, CHEM_DIF, ADV_DIF, and NET_DIF.
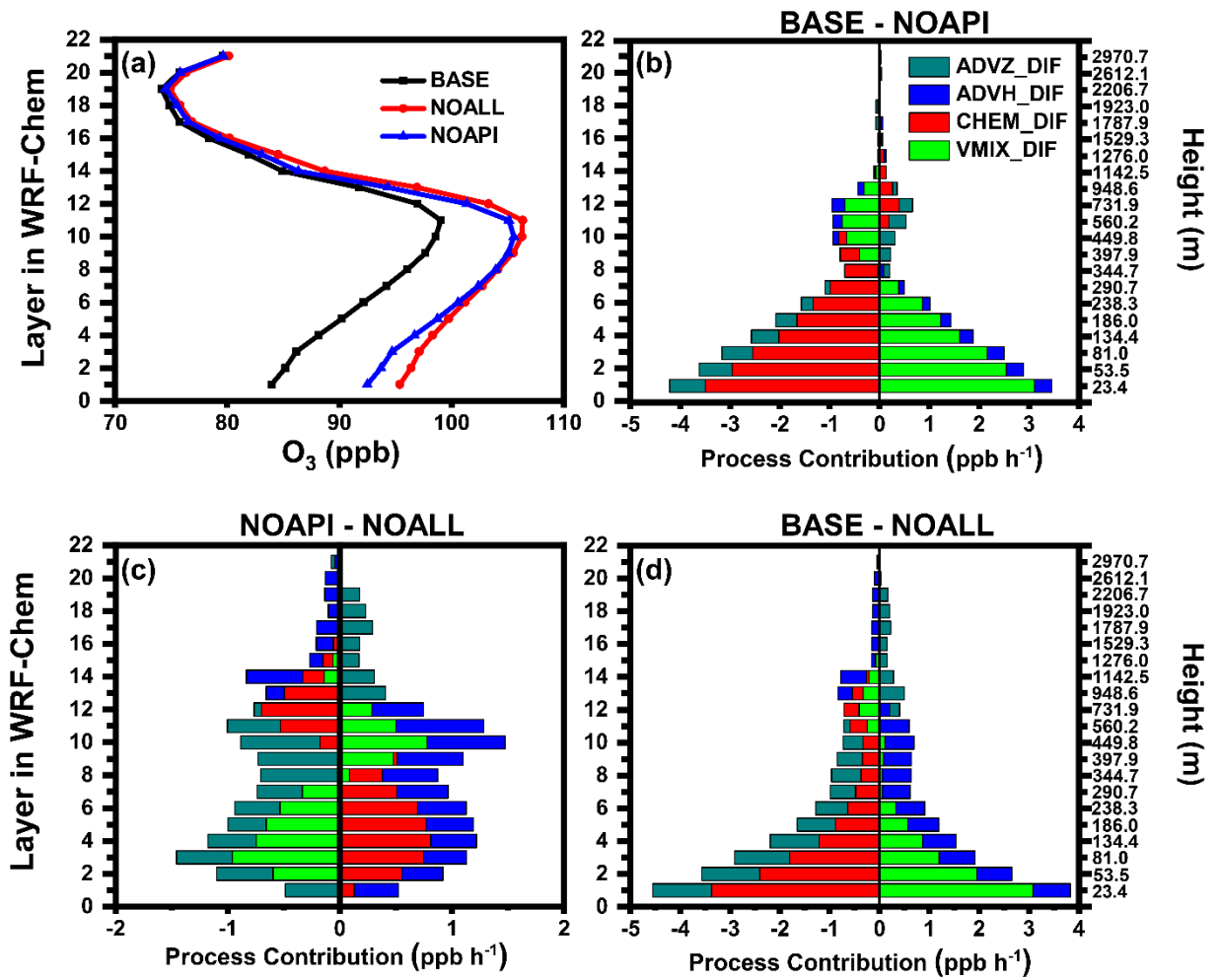
Figure 8. (a) Vertical profiles of simulated O_3 concentrations in BASE (black), NOAPI (blue), and NOALL (red) cases over CAPAs. (b-d) Changes in O_3 budget due to API, ARF, and ALL over CAPAs during the daytime (08:00-17:00 LST) from 28 July to 3 August 2014. Differences of each process contribution are denoted by ADVZ_DIF, ADVH_DIF, CHEM_DIF, and VMIX_DIF.